The Astrophysical Journal, 901:69 (12pp), 2020 September 20 https://doi.org/10.3847/1538-4357/abaaac

X-Ray Spectroscopy in the Microcalorimeter Era. II. A New Diagnostic on Column Density from the Case A to B Transition in H- and He-like Iron

P. Chakraborty, G. J. Ferland, M. Chatzikos, F. Guzmán, and Y. Su
University of Kentucky, Lexington, KY, USA
Received 2020 June 19; revised 2020 July 6; accepted 2020 July 8; published 2020 September 23

Abstract

The Soft X-ray Spectrometer on board Hitomi, with the unprecedented resolving power of $R \sim 1250$, allowed the detection of members of the Fe XXV Kα complex emission spectra from the center of the Perseus Cluster. In this paper, we introduce a novel method of measuring the column density using the optically thin (Case A) to optically thick (Case B) transition for one- and two-electron systems. We compare the Fe XXV K α line ratios computed with CLOUDY with that from the Hitomi observations in the outer region of the Perseus core using collision strengths from different atomic data sets, and obtain good agreement. We also show the effect of turbulence on Fe XXV Kα line ratios and interplay between column density and metallicity. Additionally, we discuss the atomic number dependence of transition probabilities for allowed and unallowed transitions, which causes highly charged He-like systems, such as Fe XXV, to behave fundamentally differently from He I.

Unified Astronomy Thesaurus concepts: Galaxy clusters (584); Perseus Cluster (1214); X-ray astronomy (1810); High resolution spectroscopy (2096); Radiative transfer (1335); Intracluster medium (857)

1. Introduction

Galaxy clusters are the largest gravitationally bound objects in the universe. Due to X-ray emission from the hot (10^7-10^8 K) intracluster medium (ICM), they serve as excellent probes of gas dynamics (Sarazin 2008; Elmegreen et al. 2009; McCourt 2014; Planelles et al. 2016), the cooling-heating mechanism (Peterson & Fabian 2006; Zhuravleva et al. 2014), and formation of large-scale structure (Borgani 1995; Radburn-Smith et al. 2006; Feretti et al. 2012; Tugay & Voytsehovsky 2017; Chakraborty et al. 2018). Temperature profiles of ICM in many clusters show a temperature drop toward the cluster core, the so-called cool-core clusters (Molendi & Pizzolato 2001). Radiative cooling time-scales in such clusters are significantly shorter than the Hubble time (Edge et al. 1992; White et al. 1997; Allen 2000). In principle, this should lead to a slow infall of ICM toward the cluster core, the scenario known as cooling flow (Fabian 1994). Peterson et al. (2003) found a large deficiency in the observed emission from low-temperature X-ray gas, in contrast to the prediction of the standard cooling-flow model.

There are many theories that account for this lack of cool X-ray emission. Feedback by an active galactic nucleus (AGN) is the most plausible theory to explain the suppression of cooling in the core (McNamara & Nulsen 2007). Deep Chandra observations provide evidence in favor of AGN feedback through the exchange of mechanical energy between radio-emitting jets and the ICM (Fabian 2012). This scenario is backed up by simulations (Dubois et al. 2010; Li & Bryan 2012). Perseus is the brightest X-ray cluster ($z = 0.01756$), and the prototypical cool-core cluster. Ariel 5 observations of the Fe XXV and Fe XXVI emission features near 7 keV in Perseus established that its X-ray emission comes from a diffuse hot plasma, permeating the cluster volume (Mitchell et al. 1976). Later, the Fe XXV complex was detected with XMM-Newton at 6.7 keV, and it was used to investigate for the evidence of gas motions in the Perseus core (Churazov et al. 2003, 2004).

Tremendous advancement in X-ray astronomy was made with the launch of the Hitomi Observatory on 2016 February 17. The Soft X-ray Spectrometer (SXS; Kelley et al. 2016) on board Hitomi is equipped with an X-ray microcalorimeter paired with a Soft X-ray Telescope. The microcalorimeter spectrometer provided a resolving power of $R \sim 1250$ (Hitomi Collaboration et al. 2016), allowing the detection of many weak emission/absorption lines. The previously detected Fe XXV complex in Perseus was resolved by SXS into four main components—the resonance (w), intercombination (x, y), and forbidden (z) lines (see Table 1). Also, bulk and turbulent motions of the ICM were precisely measured for the first time with the SXS from Doppler shifts and broadening of spectral lines (Hitomi Collaboration et al. 2016).

Future X-ray missions like XRISM (follow-up of Hitomi) and ATHENA will offer a plethora of high spectral resolution X-ray data. Complete computational plasma simulations are required to model several important cluster properties like temperature, turbulence, and metal abundances with high precision. In this paper, we present a study of the Fe XXV X-ray emission in Perseus based on Hitomi data with the spectral synthesis code CLOUDY (last reviewed by Ferland et al. 2017). This is a step toward achieving a precise spectral synthesis model for the above future X-ray missions.

With the advancement in spectral resolution, radiative transfer effects that are known in the optical will become accessible to X-ray astronomy. For example, in addition to optically thin line emission propagation (Case A), optically thick emission (Case B) is expected at sufficiently high column densities (Baker & Menzel 1938). This is the theme of this paper. Similar effects in the presence of a continuous radiation source (Case C, Baker et al. 1938; Ferland 1999) will be explored in a future paper.

The Case A/B/C transition is a property of all one- and two-electron systems, although most studies consider H and He in the optical because historically ground-based instruments had the highest throughputs and were able to obtain the highest resolution and signal-to-noise ratio spectra. Only now, such works are becoming possible in the X-ray emitting gas from galaxy clusters. Previous works on X-ray one-electron Case A and B include Storey & Hummer (1995) and, for two-electron systems, Porter & Ferland (2007). In this work, we use CLOUDY to simulate the

Table 1
List of Energies and Transition Probabilities for the Relevant $n = 2, 3$ to $n = 1, 2$ Transitions in Fe XXV

Label	Transition	Types	Energy (keV)	Transition Probability		
				CLOUDY	NIST	Difference
w	$2^1P \rightarrow 1^1S$	E_1	6.7007	4.54e+14	4.57e+14	1%
x	$2^3P_2 \rightarrow 1^1S$	M_2	6.6824	6.30e+09	6.64e+09	5%
y	$2^3P_1 \rightarrow 1^1S$	$E_1 + M_1$	6.6679	4.11e+13	4.42e+13	8%
z	$2^3S \rightarrow 1^1S$	M_1	6.6368	2.15e+08	2.12e+08	1%
⋯	$3^1P \rightarrow 1^1S$	E_1	7.8758	1.29e+14	1.24e+14	4%
⋯	$3^3P_1 \rightarrow 1^1S$	$E_1 + M_1$	7.8688	1.86e+13	1.50e+13	19%
⋯	$3\ ^3P \rightarrow 2\ ^3S$	E_1	1.2352	8.66e+12	8.08e+12	7%

Note. $n = 2$ levels are j-resolved in Triplet P.

environment in the outer region of the Perseus core, showing Case A to B transition in the Fe XXV and Fe XXVI emission lines. Varying the column density of the simulated cloud is what drives this transition. Surprisingly, we observe Case A to B transition in both allowed and forbidden lines in the two-electron iron.

In addition to the Case A to B transfer, another important factor contributing to the change in the emission line intensities is the loss of identity of a line photon due to line interlocking. As a result of line interlocking, a Fe XXV line photon can be absorbed by Fe^{23+}, leading to autoionization in some fraction of the absorbing ion, ultimately destroying the Fe XXV Kα photon by resonant auger destruction (Ross et al. 1996; Liedahl 2005). Another atomic process, which we call electron scattering escape (ESE), leads to the change in the Fe XXV Kα line intensities at hydrogen column densities greater than 10^{23} cm^{-2}. These two processes have been discussed in the first paper of this series, Chakraborty et al. (2020, hereafter Paper I). However, it is difficult to study these processes separately when explaining the variation of the Fe XXV Kα line intensities with column density. The prime focus of this paper is on Case A to B transfer, with occasional references to line interlocking and RAD.

This paper is organized as follows. Section 2 summarizes all the relevant atomic processes. Section 3 discusses Case A to Case B transition for hydrogen and heavier elements. Section 4 presents our X-ray analysis of the Hitomi observational data. Section 5 discusses the parameters used for our simulations with CLOUDY. Section 6 demonstrates our results: optically thin (Case A) to optically thick (Case B) transition in Fe XXV and Fe XXVI, constraints on column density, the interplay between column density and metallicity, and effect of turbulence in Perseus core from the Fe XXV line ratios. Finally, we discuss our results in Section 7. Unless otherwise mentioned, all uncertainties in this paper are reported at 3σ intervals.

2. Atomic Processes

In this section we describe the various atomic data sources we apply in our spectral modeling. Some data sources, especially collisions, are uncertain and we try to estimate this, and show their effects on the spectrum.

2.1. Energy Levels

Helium energy levels are taken from Martin & Wiese (2006). Energy levels for heavier He-like ions, lithium through zinc, are taken from the CHIANTI atomic database version 5 (Dere et al. 1997; Landi et al. 2005).

We use j-resolved levels for the $2\ ^3P$ terms in order to calculate accurate populations for these levels, and emissivities

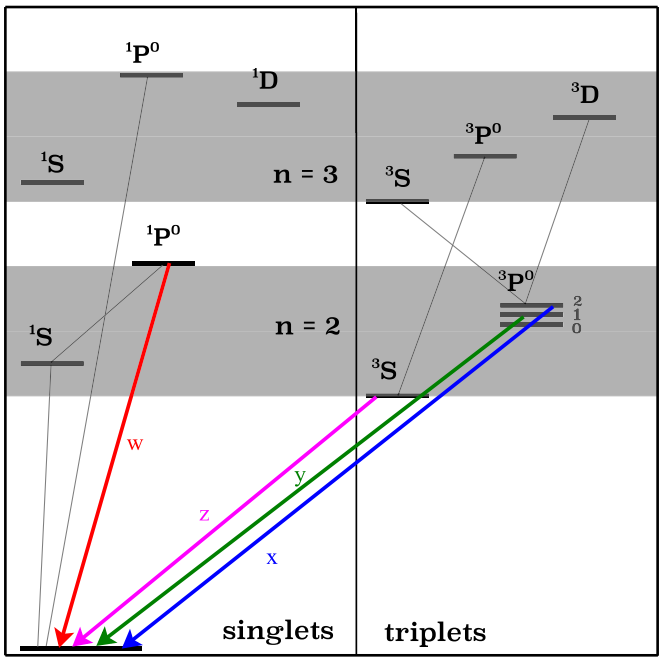

Figure 1. Grotrian diagram (not to scale) for He-like ions ($Z \geqslant 10$). Note that the relative order of the energy levels is different at lower ionic charges. x, y, z, and w transitions are marked with blue, green, purple, and red, respectively.

for the intercombination lines between them and the ground state. We include *nls* resolved levels for $n \leqslant 5$ (where n is the principal quantum number), while levels in the range $5 \leqslant n \leqslant 100$ are collapsed (see Figure 1 in Ferland et al. (2013) for a schematic representation of resolved and collapsed levels). The energy levels of He-like ions are represented in Figure 1. In Table 1, there is a list of transition energies from $n = 2, 3 \rightarrow n = 1$ for Fe XXV in the interval of 6.5–8.0 keV.

2.2. Radiative Transition Rates

Porter & Ferland (2007) list all the sources of $n = 2, 3$ to $n = 2, 1$ transition probabilities used in CLOUDY. We show the dependence of transition probabilities for $2\ ^1P \rightarrow 1\ ^1S$, $2\ ^3P \rightarrow 1\ ^1S$, $2\ ^3S \rightarrow 1\ ^1S$, $3\ ^1P \rightarrow 1\ ^1S$, and $3\ ^3P \rightarrow 1\ ^1S$ transitions on atomic number (Z) in Figure 2. The significance of this figure will be discussed in Section 3.3.

Table 1 gives a comparison between transition probabilities from CLOUDY and NIST[1] (version 5.6.1: Kramida et al. 2018). They show an agreement within 8% for $n = 2$ to $n = 1$

[1] https://physics.nist.gov/asd

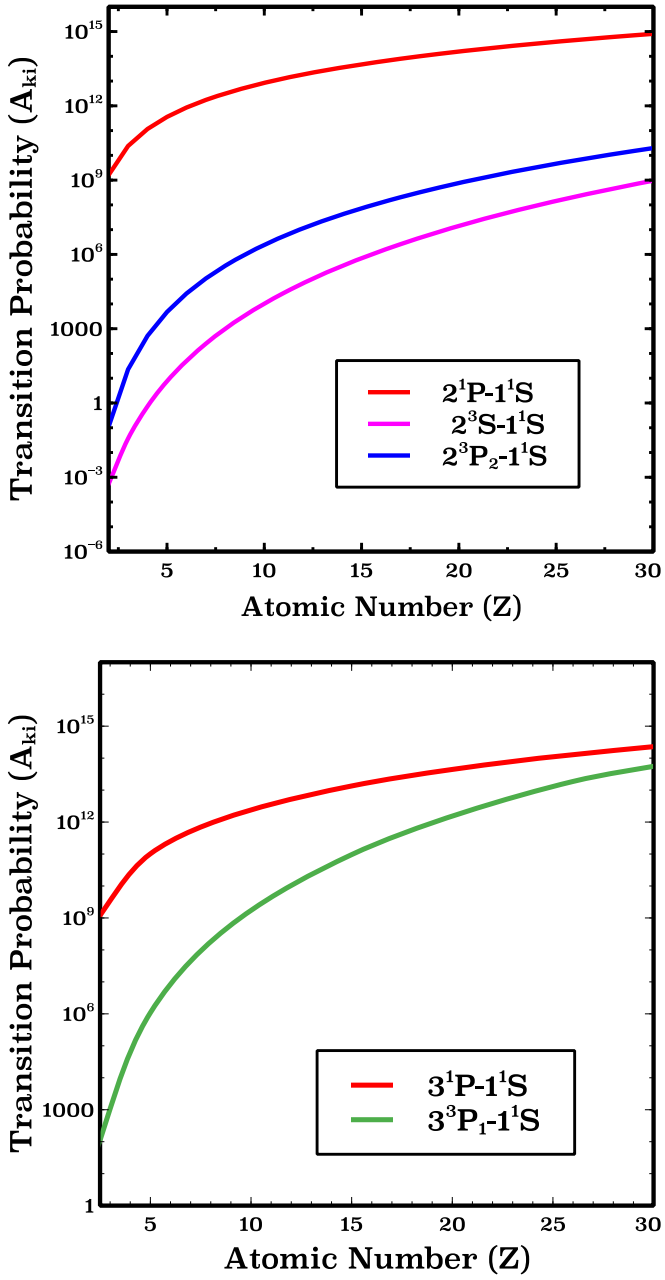

Figure 2. Top: transition probabilities vs. Z for certain $n = 2$ to $n = 1$ transitions for He-like ions. Bottom: transition probabilities vs. Z for certain $n = 3$ to $n = 1$ transitions.

transitions, but a variation up to 19% for $n = 3$ to $n = 1$ transitions.

2.3. Recombination Rate Coefficients

Coefficients for radiative recombination rates are calculated from photoionization cross sections using the Milne relation (Osterbrock & Ferland 2006). Photoionization cross sections for the ground state of He-like ions are taken from Verner et al. (1996), which uses analytic fits from the Opacity Project. Dielectric recombination data are interpolated from Badnell (2006). See Porter & Ferland (2007) and Ferland et al. (2013, 2017) for a discussion on state-specific recombination rates.

2.4. Collisional Data

2.4.1. Electron Impact n-changing Collisions

We interpolate the collision strengths from various atomic data sets for the right temperature (see Section 6) for $n = 2$–$5 \rightarrow 1$ transitions of Fe^{24+}. For higher n and Rydberg levels, we use the ab initio Born approximation theory by Lebedev & Beigman (1998), following the analysis in Guzmán et al. (2019).

2.4.2. Electron Impact Bound–Free Collisions

We take collisional ionization rate coefficients from Voronov (1997) for the ground state. For excited states, rate coefficients are taken from the hydrogenic routines of Allen (1973) for the lower temperatures, and from Sampson & Zhang (1988) at the high-temperature end.

3. The Case A and B Framework in Atoms and Highly Charged Ions

3.1. Introduction to Case A and B, H I Optical Emission

Case A and Case B have been defined for hydrogen emission (Baker & Menzel 1938; Osterbrock & Ferland 2006). Case A refers to an optically thin plasma where Lyman radiation is transmitted without absorption (Osterbrock & Ferland 2006). At low hydrogen column density, all line photons emitted escape the cloud.

Case B occurs when the ionized cloud becomes optically thick to the H I Lyman resonance lines, due to high hydrogen column density. The Lyman photons undergo multiple scatterings and are degraded to lower-energy photons (page 70–71, Osterbrock & Ferland 2006). For instance, after approximately nine scatterings, a Lyβ photon gets degraded to a Hα photon plus two-photon continuum. Line formation in most nebulae can be explained by conditions closer to Case B. In this limit, the electron density must be small enough ($n_e \leqslant 10^8$ cm^{-3}) for the collisional deexcitation rate to be lower than spontaneous emissions (Hummer & Storey 1987).

3.2. Atomic Helium

Radiative lifetimes for excited helium atoms range between less than a nanosecond to several minutes. For example, $2\,^1P_1$ decays to the ground state in 0.56 ns, which is very short compared to the decay times in $2\,^3P_2$ (3.05 s) and the metastable $2\,^3S$ levels (131 minutes). These are respectively examples of E_1 (electric dipole), M_2 (magnetic quadrupole), and M_1 (magnetic dipole) transitions for $n = 2 \rightarrow 1$. The decay of $2\,^3P_1$ to the ground state has a radiative lifetime of $\sim$5.68 ms and is a combination of E_1 and M_1 (Kunze 2009).

In Figure 2 we plot transition probabilities for He-like ions with $2 \leqslant Z \leqslant 30$. From the figure it is clear that in helium, there is no fast transition to the ground from excited triplet states due to their longer radiative lifetimes (and smaller transition probabilities ($A_{u,l}$)). Optical thickness is proportional to the absorption cross section at frequency ν (α_ν), which is proportional to $A_{u,l}$ (refer to Equations (2) and (3)). Therefore, for helium, there will be no Case A (optically thin) to Case B (optically thick) transition for triplet to ground transitions. Fast transitions only occur in the allowed singlet to singlet transitions (E_1) with decay times of the order of nanoseconds and large absorption cross sections, thus allowing for Case A to

B transitions. This is not the case, however, for higher atomic numbers. Atomic number dependence of transition probability for allowed and forbidden transitions will be discussed in Section 3.3.

3.3. X-Ray Emission from He-like Fe XXV

Along the two-electron isosequence, the next abundant elements are C, O, and N, emitted in soft X-rays and discussed by Porter & Ferland (2007). This paper continues to iron, inspired by recent Hitomi observations of the Fe Kα complex in the Perseus galaxy cluster.

In Fe XXV, in contrast to the atomic helium discussed in Section 3.2, triplet to singlet transitions can also become optically thick (Case B) along with the singlet to singlet transitions. This is surprising at first sight, but can be explained with the transition probability (A_{ki}) dependence on the atomic number (Z) for different types of transitions.

Probabilities for E_1 transitions ($2\ ^1P - 1\ ^1S$ (w), $3\ ^1P - 1\ ^1S$) grow with the fourth power of Z ($A_{ki} \propto Z^4$, Johnson et al. 2002), whereas transition probabilities for M_1 ($2\ ^3S - 1\ ^1S$ (z)) and M_2 ($2\ ^3P_2 - 1\ ^1S$ (x)) grow much faster with Z (approximately $\propto Z^{10}$ and $\propto Z^8$, Lin et al. 1977). The transition probabilities for $2\ ^3P_1 - 1\ ^1S$ (y) and $3\ ^3P_1 - 1\ ^1S$ are a combination of E1 and M1, and also grow much faster than the allowed E_1 transitions. Therefore, in higher Z ions like iron, transition probabilities ($A_{u,l}$), and the optical depths for some of the triplet to singlet transitions become comparable to that of the allowed singlet to singlet transitions (see Figure 2). This implies that Case A to B transition occurs in singlet to singlet as well as triplet to triplet transitions in Fe XXV and other higher Z He-like ions.

3.4. X-Ray Emission from H-like Fe XXVI

Unlike helium, there is no fundamental difference between atomic hydrogen and the highly charged H-like ions. This point is elaborated in Section 6.1.2.

4. Line Ratios from Hitomi Observations

The observational spectra for the Fe XXV Kα are extracted using HEAsoft version 6.25[2] in the outer region of Perseus core following the Hitomi step-by-step analysis guide.[3] We use the following observations with observation IDs: 100040020, 100040030, 100040040, and 100040050 for extracting the spectra for the region marked with Obs23:out in Hitomi Collaboration et al. (2018a; we show this region in Figure 3). Event files for these observations are combined and filtered with the Xselect package. Four NXB spectra are extracted separately for the four event files with `sxsnxbgen`, and averaged using `mathpha`. RMF, exposure map, and ARF were generated using `sxsmkrmf`, `ahexpmap`, and `aharfgen`, respectively. For fitting the spectra, we use Xspec version 12.10.1 (Arnaud 1996).

The X-ray emission from our region of interest was modeled as a velocity-broadened single-temperature collisionally ionized plasma with variable element abundances (`bvvapec`), attenuated by the cold matter absorption in our Galaxy (`TBabs`). The absorbing hydrogen column density was set to

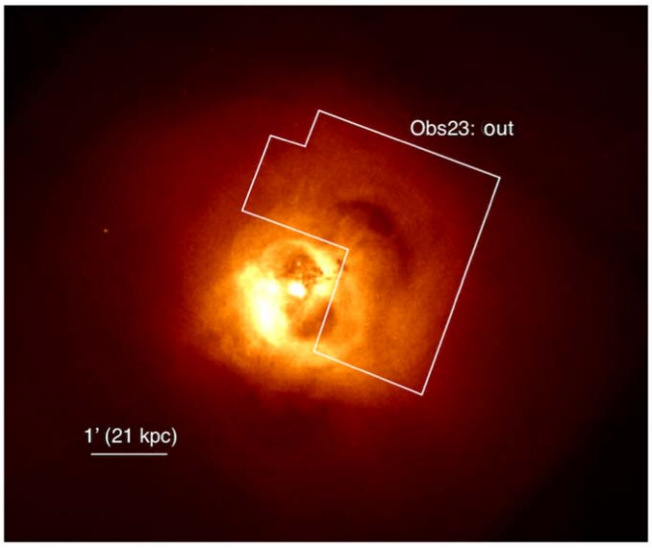

Figure 3. The outer region of the Perseus core from Hitomi SXS observation (marked with Obs23: out) overlaid on a Chandra X-ray image of Perseus.

1.38×10^{21} cm^{-2} (Leiden/Argentine/Bonn Survey of Galactic H I: Kalberla et al. 2005). The `bvvapec` model was modified whenever necessary by setting the emissivities to zero for selected lines, following the addition of corresponding Gaussian components. The contamination by the central AGN emission is negligible in the outer region; thus such effects were not included in our model.

We use the outer region temperature (4.05 ± 0.01 keV), Fe abundance (0.65 ± 0.01), and turbulent velocity (141 ± 5 km s^{-1}) from a broadband fit in the energy range 1.8–20.0 keV from Hitomi Collaboration et al. (2018a; errors are reported at the 1σ confidence level). The solar abundance table by Lodders & Palme (2009) was used throughout. For calculating the line fluxes for x, y, z, and w, we set the line emissivities for these lines to zero, and add four Gaussians with energies centered at their redshifted laboratory energies ($E_{0x} = 6.68245$ keV, $E_{0y} = 6.66790$ keV, $E_{0z} = 6.63684$ keV, $E_{0w} = 6.70076$ keV). In the modified `bvvapec` model: `tbabs`*(`bvvapec` + `zgauss`$_x$ + `zgauss`$_y$ + `zgauss`$_z$ + `zgauss`$_w$), we tie the line widths of x, y, z together, and set the line width for w free to vary. This is because w is reported to be slightly broader than the other three lines in Fe XXV Kα complex (Hitomi Collaboration et al. 2018a). The normalizations of the four Gaussians were set free, and redshifts were tied together. Our best-fit model for the observed spectra for Fe XXV Kα complex from Obs23:out is shown in Figure 4 with a black solid line. The red, blue, green, and purple dotted lines show the four Gaussians for w, x, y, and z, respectively. The black dotted line shows the `bvvapec` model with x, y, z, and w emissivities set to zero. Under such conditions, major contributions to the `bvvapec` model come from Fe XXIV satellite lines, following the contributions from Cr XXIII, and Fe XXIII in the energy range of the figure. The best-fit redshift for our model is $z = 0.0173308^{+2.53e-05}_{-2.46e-05}$. The best-fit parameters for the four Gaussians and line fluxes with the line ratios are listed in Tables 2 and 3, respectively.

5. Simulation Parameters

For the CLOUDY calculations, we simulate the environment in the outer region of the Perseus core, introduced as Obs23:out

[2] https://heasarc.gsfc.nasa.gov/docs/software/heasoft/

[3] https://heasarc.gsfc.nasa.gov/docs/hitomi/analysis/hitomi_analysis_guide_20160624.pdf

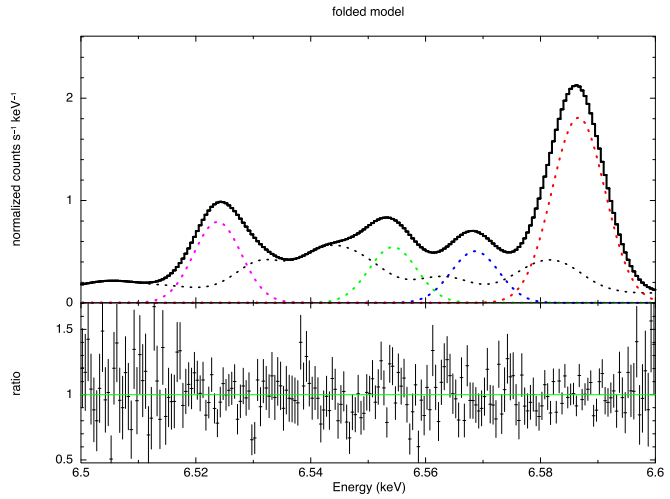

Figure 4. The black solid line shows the best-fitting model with x, y, z, w emissivities set to zero, and four added Gaussians centered at their redshifted laboratory energies. Red, blue, green, and purple dotted lines show the four Gaussians for w, x, y, and z separately. The black dotted line shows the `bvvapec` model without x, y, z, and w.

Table 2
Best-fit Normalization and σ of the Four Gaussians from Our Model: `tbabs*(bvvapec + zgauss`$_x$ `+ zgauss`$_y$ `+ zgauss`$_z$ `+ zgauss`$_w$`)`

Label	Normalization ($\times 10^{-5}$ photons/cm^{-2}/s)	Sigma (keV)
x	$9.80^{+0.92}_{-0.88}$	$3.61e{-}03^{+2.78e-04}_{-2.63e-04}$
y	$10.56^{+1.03}_{-0.98}$	$3.61e{-}03^{+2.78e-04}_{-2.63e-04}$
z	$15.34^{+1.10}_{-1.07}$	$3.61e{-}03^{+2.78e-04}_{-2.63e-04}$
w	$39.22^{+1.56}_{-1.52}$	$4.17e{-}03^{+1.94e-04}_{-1.87e-04}$

Note. Temperature, Fe abundance, and turbulent velocity in the `bvvapec` model are set to the values from broadband fits in Obs23:out. Line emissivities of x, y, z, and w are set to zero.

in Section 4. We choose the temperature inside the error interval of the observation: $4.05^{+0.01}_{-0.01}$ keV. The hydrogen density is set at 0.03 cm^{-3}. Note that the hydrogen density drops with increasing distance from the cluster core. For simplicity, we assume an average hydrogen density of 0.03 cm^{-3} for our region of interest (30–60 kpc). The radial dependence of hydrogen density will be explored in future papers.

We set the Fe abundance to be in the range of $0.65^{+0.01}_{-0.01}$ of solar, as discussed in Section 4. Sections 6.4, where we show the variation of line ratios with changing metallicity, is an exception. We use the solar abundance table provided by Lodders & Palme (2009) to match with Hitomi Collaboration et al. (2018a). The turbulence is set to 150 km s^{-1} (this choice is elaborated later in Section 6.3) for all our calculations except for Section 6.3, where we use two additional values for turbulence. In Section 6.3 and partly in Section 6.4, hydrogen column density is fixed at the reported value by Hitomi Collaboration et al. (2018b) ($N_{\rm H,hot} \sim 1.88 \times 10^{21}$ cm^{-2}). This is the column density of hot absorbing gas, derived from a best-fit baseline model defined with SPEX (Kaastra et al. 1996). In their model $N_{\rm H,hot}$ is set as a free parameter, along with temperature and turbulent velocity of hot gas, emission measure, redshift, and abundances of Si, S, Ar, Ca, Cr, Mn, Fe, and Ni.

For the collision strengths, we use the recent calculations of Si et al. (2017), who adopted the independent process and isolated resonance approximations using distorted waves. Since we find instances of disagreement between observed and calculated line ratios, we also check the effect of different atomic data sets on the calculated line ratios (such as Figures 5 and 6). These include collision data from Whiteford et al. (2001), A. D. Whiteford (2005),[4] and A. Giunta (2012).[5] Hitomi Collaboration et al. (2018a) shows the presence of resonance scattering (RS) in the Perseus core, which results in flux suppression in w. In the outer region (Obs23:out), the flux suppression factor in w is reported to be ∼1.28. We make a correction for this factor for our calculations, as we use a simple model with plane-parallel geometry that does not account for the photons lost due to RS in our line of sight. This will be further discussed in Section 7.

6. Results

6.1. Case A and Case B in Iron

6.1.1. Fe XXV

The Case A to B transition happens when the total line-center optical depth of the Lyman lines becomes ⩾1. Note that the variation in optical depth is determined by the column density of that species, Fe XXV, in this case. The column density of Fe^{24+} ($N(Fe^{24+})$) can be calculated from the hydrogen column density (N(H)) for a given metal abundance (Fe/H), and ionization fraction (Fe^{24+}/Fe) with the following equation:

$$\mathrm{N(Fe^{24+})} = \left(\frac{\mathrm{Fe^{24+}}}{\mathrm{Fe}}\right)\left(\frac{\mathrm{Fe}}{\mathrm{H}}\right) N(\mathrm{H}). \quad (1)$$

This conversion is shown in the top x-axes in Figures 7, 8, and 9.

Decay rates in Fe^{24+} for triplet to singlet and singlet to singlet transitions are comparable to each other for some transitions, as discussed in Section 3.3. This allows the transfer from the optically thin (Case A) to the optically thick regimes (Case B) for singlet to singlet, as well as triplet to singlet transitions.

Figure 10, taken from Paper I, shows the line intensities for x, y, z, and w in the Fe XXV Kα complex. The continuous increase in the line intensities with column density makes it difficult to detect where the Case A to B transition occurs for the individual spectral lines. To demonstrate the Case A to B transition, it is best to consider the variation of line ratios with column density. Among the four members in the Fe XXV Kα complex, w is the first line to become optically thick, followed by y, x, and z (Refer to Figure 1(b) in Paper I). z only becomes optically thick at very high column densities ($N_{\rm H} \geqslant 10^{25}$ cm^{-2}). The figure also gives an estimate of what fraction of the optical depth for the four lines comes from their single-line optical depth solely (in this case absorption by Fe^{24+} only). The total line-center optical depths in x, y, z, and w respectively have ⩽1%, ∼60%, ⩽1%, and ∼100% contribution from absorption by Fe^{24+}. As z is the last line to become optically thick, we plot line ratios of x, y, and w relative to z with hydrogen column density (see Figure 7).

[4] ADF04, OPEN-ADAS database, helike_adw05#fe24.dat, website: https://open.adas.ac.uk/.
[5] ADF04, ls#fe24.dat, OPEN-ADAS database.

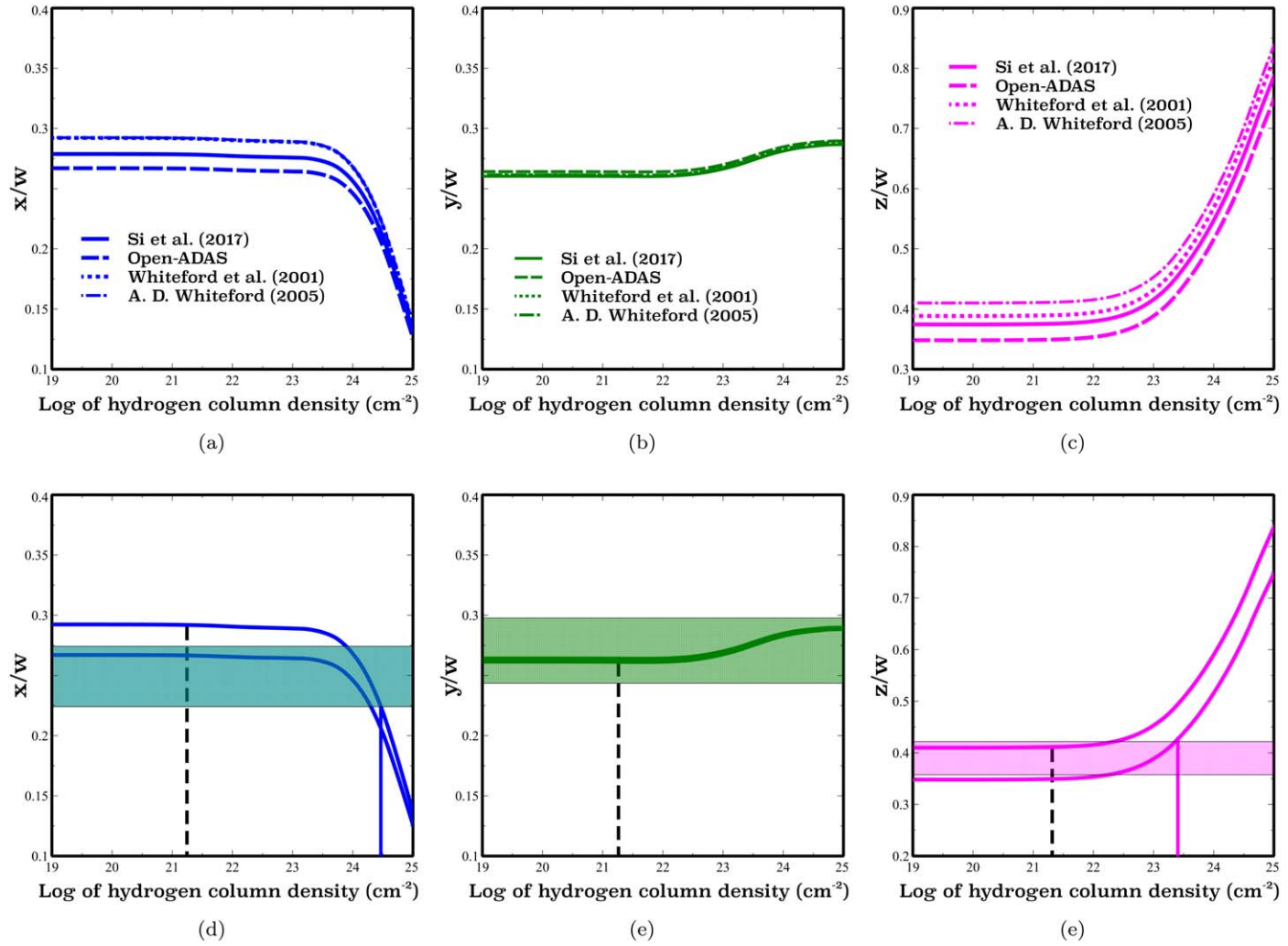

Figure 5. Variation of x/w, y/w, and z/w line ratios with hydrogen column density. Top panel: line ratios calculated with CLOUDY for different collision data sets. Bottom panel: line ratios calculated with CLOUDY with their net uncertainties overplotted with the Hitomi observed line ratios. The solid vertical lines show constraints on column density. The Hitomi reported hydrogen column density is shown with black dashed lines in each panel.

Table 3
List of Net Line Fluxes and Ratios with w for the Lines in Fe XXV Kα Complex from the Best-fit Model

Label	Line Flux	Flux Error (Positive)	Flux Error (Negative)	Ratio with w	Positive Error	Negative Error
x	1.01e−12	9.46e−14	9.14e−14	0.249	2.50e−02	2.47e−02
y	1.09e−12	1.08e−13	9.98e−14	0.268	2.91e−02	2.63e−02
z	1.57e−12	1.13e−13	1.09e−13	0.387	3.13e−02	3.11e−02
w	4.06e−12	1.61e−13	1.58e−13	…	…	…

Note. Line fluxes and their errors are reported in units of erg cm^{-2} s^{-1}.

In the lower column densities, the lines ratios are parallel to each other and remain constant with increasing column density. This is because the individual line intensities are all parallely increasing when the column density, and therefore optical depth, is small (Case A).

At higher column densities (Case B limit), the figure shows an overall decrease in w/z, x/z, and y/z, which can be caused by the decrease in the numerator, or increase in the denominator, or a combination of these two. In between these two cases, there is a transition region representing the transfer from Case A to Case B.

The probability that an x photon gets absorbed by Fe^{24+} itself is $\leqslant$1%. The effect of Case A to B transfer in x following absorption by Fe^{24+} is therefore very minimal. Apart from this, contributions from RAD and ESE cause a deficit in the x line intensity (Paper I).

Unlike x, the total line-center optical depth in y has a ∼60% contribution from absorption by Fe^{24+} itself. When a y photon gets absorbed by Fe^{24+}, it leads to two possible modes of re-emission. It can either be re-emitted as a y photon or make a transition to $2\,^3S$ following the emission of a z photon. The probability of re-emission via either of these modes depends on

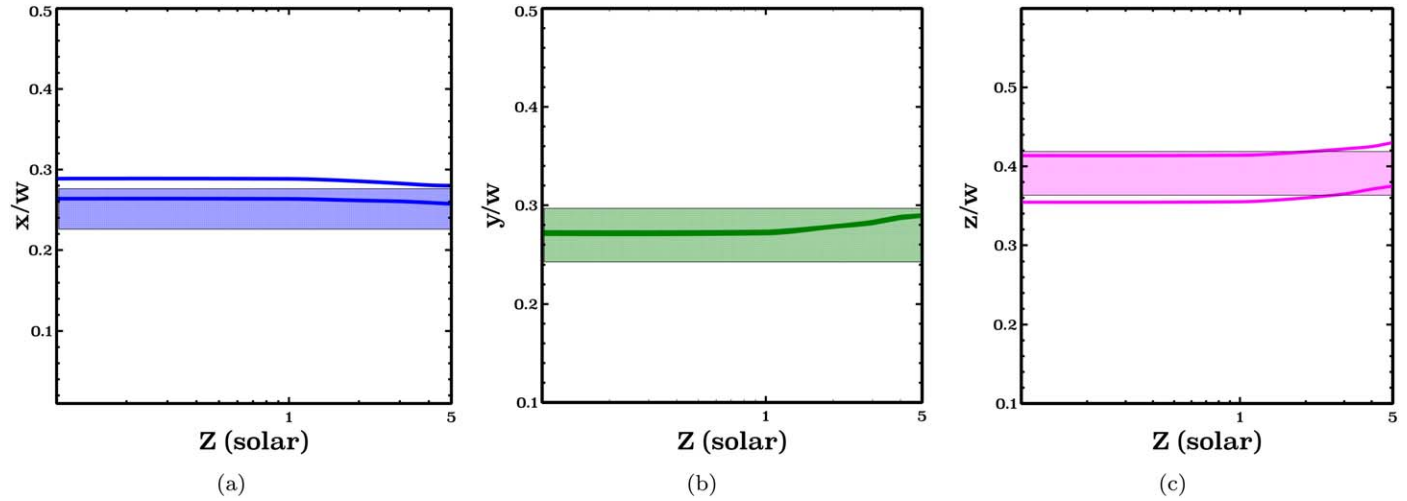

Figure 6. Line intensity ratios vs. metallicity at $N_{\rm H} = 1.88 \times 10^{21}\,{\rm cm}^{-2}$. The blue, green, and purple lines in the left, middle, and right panels enclose the x/w, y/w, and z/w calculated with CLOUDY. The enclosed regions are inclusive of the uncertainty in temperature, and different collision data sets. Observed line ratios with errors are shown with the horizontal bars in all three panels.

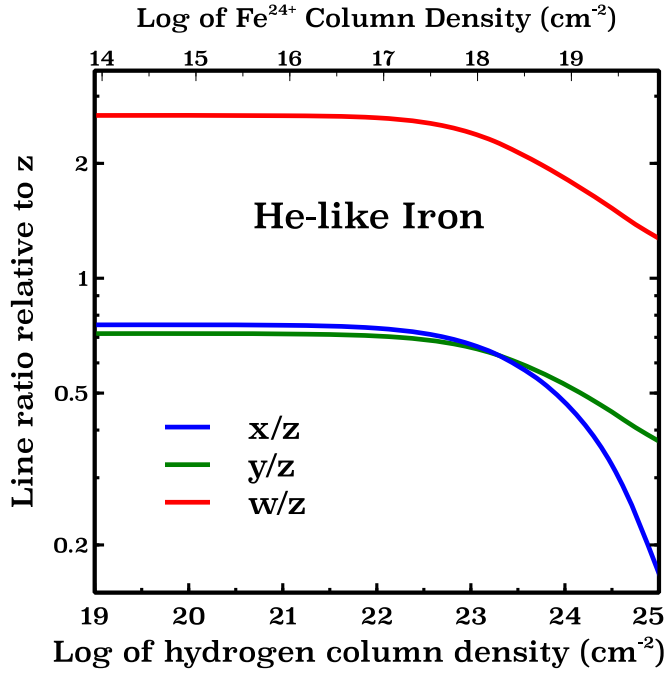

Figure 7. Fe XXV line ratios with respect to z for $2 \rightarrow 1$ transitions vs. log of hydrogen column density. The *x*-axis on top shows log of Fe^{24+} column density.

the transition probabilities between the levels or, more specifically, branching ratios. The branching ratio for the scattered y photon being re-emitted as a $2\,^3P_1 \rightarrow 2\,^3S$ following a z transition is quite small:

$$\frac{A_{2\,^3P_1 \rightarrow 2\,^3S}}{(A_{2\,^3P_1 \rightarrow 2\,^3S} + A_{2\,^3P_1 \rightarrow 1\,^1S})} \sim 10^{-5}.$$

Therefore, the majority of the scattered y photons will be re-emitted as y with no decrease in y intensity. This indicates a possible increase in z intensity, causing the slower drop of the y/z ratio with increasing column density in Figure 7.

Similarly, ~100% of w photons are scattered by Fe^{24+}. Upon being scatted, there are two possible modes of re-emission for w photos. The branching ratio for $2\,^1P \rightarrow 2\,^1S$ following the transition to the ground is very small:

$$\frac{A_{2\,^1P \rightarrow 2\,^1S}}{(A_{2\,^1P \rightarrow 2\,^1S} + A_{2\,^1P \rightarrow 1\,^1S})} \sim 10^{-6}.$$

Therefore, almost all the scattered w photons will be re-emitted as w. The drop in the w/z ratio in Figure 7 mostly results from an increase in z intensity apart from the RS effects in w at large column densities.

Even though none of the $n = 2 \rightarrow 1$ photon takes part in the Case A to B transfer, higher *n* Lyman lines ($n = 3, 4, 5 \ldots \rightarrow 1$) show such transfer. The factor contributing to the increase in z is Case A to B transfer in $n = 3, 4, 5 \ldots \rightarrow 1$ photons. In an optically thick cloud, these photons are scattered, followed by emission of Balmer line photons plus the $n = 2 \rightarrow 1$ photons. This results in a surplus of $n = 2 \rightarrow 1$ photons. Tables 4.1 and 4.2 in Osterbrock & Ferland (2006) show the Case A and Case B limit in HI recombination lines. Here we discuss the increase in z intensity due to this process, whereas the slight increase in y intensity will be discussed in Section 6.2.

Case A to B transfer for $3^3P \rightarrow 1^1S$ transition is shown in the upper panel of Figure 8. The lower panel shows Case A to B transition in $n = 4, 5, 6, 7, 8, 9, 10 \rightarrow 1$ photons. A plot similar to that of 1b in Paper I is shown in Figure 9 comparing the single-line and total line-center optical depths for $3\,^3P \rightarrow 1\,^1S$ transition. The line ratios in Figure 8 are taken relative to z for the reason explained previously.

Once a photon for the $3\,^3P \rightarrow 1\,^1S$ transition gets scattered, the probability that it will emit a $3\,^3P \rightarrow 2\,^3S$ following the emission of a $2\,^3S \rightarrow 1\,^1S$ (z) photon is ~32% in one scattering:

$$\frac{A_{3\,^3P \rightarrow 2\,^3S}}{(A_{3\,^3P \rightarrow 2\,^3S} + A_{3\,^3P \rightarrow 1\,^1S})} \sim 0.32.$$

Therefore, for a single event of scattering, $3\,^3P \rightarrow 1\,^1S$ photons have a 32% probability of being converted to z and Balmer series line photons. At a hydrogen column density of $N_{\rm H} = 10^{25}\ {\rm cm}^{-2}$, the triplet to singlet transition photons will experience multiple scatterings because of their large optical

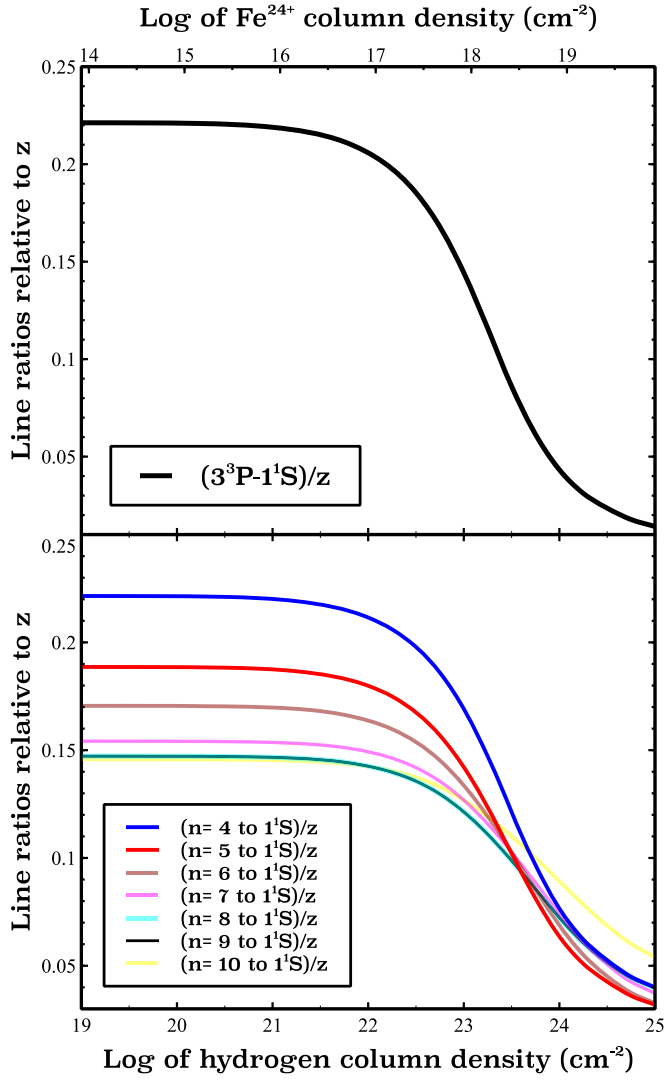

Figure 8. Upper panel: Fe XXV line ratios with respect to z for $3\ ^3P \rightarrow 1\ ^1S$ transition vs. log of hydrogen column density. Lower panel: Fe XXV line ratios with respect to z for $n = 4, 5 \ldots \rightarrow 1\ ^1S$ transitions vs. log of hydrogen column density. The x-axis on top shows log of Fe^{24+} column density.

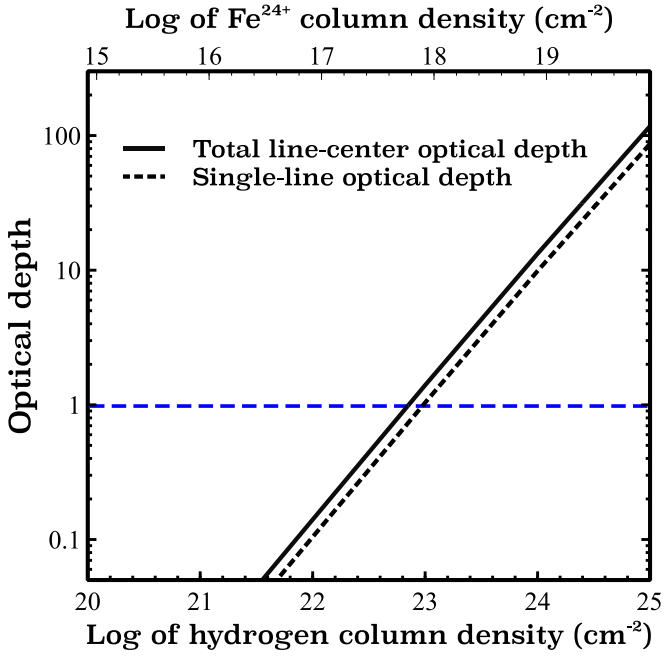

Figure 9. Optical depth vs. hydrogen column density for $3\ ^3P \rightarrow 1\ ^1S$ transition in Fe XXV. Solid: total line-center optical depth. Dotted: individual line optical depth. The x-axis on top shows log of Fe^{24+} column density. The blue dashed line marks the optical depth of unity.

depths (∼100; see Figure 9). The majority of these line photons will be converted to z and Balmer series photons at this column density. This contributes to the increase in the intensity of z line photons in Figure 7, and a decrease in the intensity of $3\ ^3P \rightarrow 1\ ^1S$ line photons in the top panel of Figure 8. Likewise, $n = 4, 5 \ldots 10 \rightarrow 1$ transition-line photons show a similar behavior indicating a Case A to B transfer (bottom panel of Figure 8), and selectively contribute to the increase in z intensity. Although we show the Case A to B transfer of Lyman line photons up to $n = 10$, we include collapsed levels up to $n \leqslant 100$ in our simulation. The net increase in the z line intensity will result from the collective Case A to B transfer of Lyman line photons for transitions from all the levels up to $n = 100$.

6.1.2. Fe XXVI

As mentioned in Section 3.4, there is no fundamental difference between Fe^{25+} and other hydrogenic ions. We show the Case A to B transition for the line intensity ratios Lyβ, Lyγ, Hα, and Hβ with respect to Lyα in Figure 11 (Lyα, Lyβ, Lyγ, Hα, and Hβ are $n = 2 \rightarrow 1$, $n = 3 \rightarrow 1$, $n = 4 \rightarrow 1$, $n = 3 \rightarrow 2$, and $n = 4 \rightarrow 2$ transitions with wavelengths 1.78177 Å, 1.50337 Å, 1.42541 Å, 9.62154 Å, and 7.12706 Å, respectively). The bottom and top axes in the figure, respectively, show the hydrogen and Fe^{25+} column densities. Line ratios are plotted instead of the individual line intensities for the same reason as discussed in Section 6.1.1.

Figure 11 shows that line ratios remain unchanged at small column densities when the lines are optically thin (Case A). But at higher column densities, the cloud becomes optically thick, the spectrum goes to Case B, and the higher n Lyman lines like Lyβ and Lyγ degrade to Hα, and Hβ, respectively. This causes the Lyman lines to become weaker, and the Balmer lines to become stronger. Such analysis can be extended to other hydrogenic ions like Si XIV, S XVI, Ar XVIII, and Ca XX for constraining/measuring column density. This will be explored in future papers.

6.2. Constraints on Column Density

We run a line ratio diagnostic for Fe XXV Kα complex with column density using the Case A to B transition. Here we plot the variation of Fe XXV line ratios (RS corrected) relative to the strongest resonance (w) line with increasing hydrogen column density in Figure 5.

At lower column densities, lines ratios remain constant with the increase in column density. Apart from the RS effects at the higher column densities, line intensities in w increase linearly, while z and x increase faster and slower than linear, respectively. The behavior of x line intensity with column density is discussed in Paper I. Faster than linear growth in z is due to the Case A to B transfer in selective $n = 3, 4 \ldots \rightarrow 1$ photons (see Section 6.1.1).

Similar to the increase in z/w, the slight increase in y/w in the high column density can also be explained with Case A to

B transfer in $n = 3, 4 \ldots \rightarrow 1$ line photons to generate Balmer line photons plus the $n = 2 \rightarrow 1$ transition photons. Such transition makes all the $n = 2 \rightarrow 1$ transitions brighter in the Case B limit compared to Case A. This process strengthens the weak $n = 2 \rightarrow 1$ transitions more than w, the strongest, leading to the slight rise in y/w at the high-column-density limit.

The top panel of Figure 5 shows the variation of line ratios relative to w with hydrogen column density for different collision data sets. The bottom panel of the figure compares the variation in line ratios calculated with CLOUDY with the observed line ratios to get the constraints on column density. The shaded horizontal regions are the observed line ratios with their uncertainties at the reported column density by Hitomi Collaboration et al. (2018b). Section 4 describes the extraction of line ratios along with their errors from the observed spectra. The regions between the two solid lines in all three panels enclose the calculated line ratios with CLOUDY. The enclosed regions are inclusive of the uncertainty in temperature and collision strengths coming from different collision data sets. Refer to Table 4 for the uncertainties in collision data sets.

The intersection regions between observed and calculated line ratios for x/w and z/w predict a hydrogen column density of $N_{\rm H} \leqslant 2.95 \times 10^{24}$ cm^{-2}, and $N_{\rm H} \leqslant 2.75 \times 10^{23}$ cm^{-2}, respectively. The solid vertical lines in the bottom panel of Figure 5 show the upper limit of column density from these two ratios. The y/w ratio calculated with CLOUDY intersects with the observed value for all column densities below 10^{25} cm^{-2}. These upper limits calculated from x/w, y/w, and z/w ratios are all consistent with the reported hydrogen column density $N_{\rm H,hot} \sim 1.88 \times 10^{21}$ cm^{-2} (shown with the black vertical dashed lines) for Perseus.

6.3. Effects of Turbulence

In Figure 12, we show the effect of turbulence on the Fe XXV Kα complex line ratios. Hitomi Collaboration et al. (2018a) found a difference in turbulent broadening between w (159–167 km s^{-1}), and x, y, z (136–150 km s^{-1}) in Obs23: out. We use a turbulent velocity of 150 km s^{-1} for simplicity in our simulation of the outer region of Perseus core. Figure 12 shows that such a quiescent gas environment barely affects the line ratios, as the difference in the line ratios calculated at the turbulence 0 and 150 km s^{-1} is very small.

We also plot the line ratios at the turbulence of 500 km s^{-1}. Such a high value of the turbulence is not applicable in our region of interest, but may apply for gas in other environments such as merging galaxy clusters (Cassano & Brunetti 2005).

Optical depth can be expressed as a product of column density (N), and absorption cross section (α_ν):

$$\tau_\nu = N\alpha_\nu \tag{2}$$

where α_ν is inversely proportional to the total Doppler velocity.

$$\alpha_\nu(x) = \frac{\lambda^3 g_u}{8\pi g_l}\frac{A_{u,l}}{\pi^{1/2}u_{\rm Dop}}\varphi_\nu(x)$$
$$= \frac{\pi^{1/2}q_e^2\lambda f_{l,u}}{m_e c u_{\rm Dop}}\varphi_\nu(x)[{\rm cm}^2] \tag{3}$$

where $A_{u,l}$ is the downward transition probability, $f_{l,u}$ is the oscillator strength and other symbols have their usual meaning (Mihalas 1970). If the temperature is held constant, an increase in the turbulent velocity decreases α_ν, which decreases the overall optical depth.

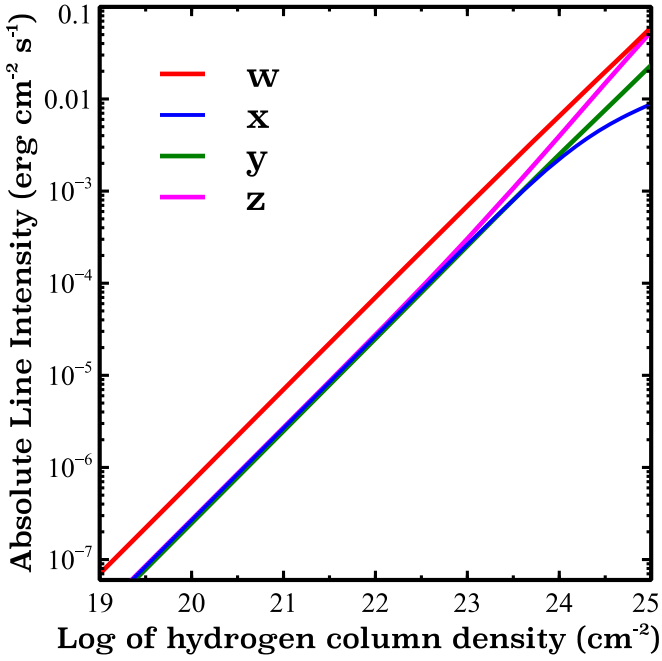

Figure 10. Absolute line intensities of x, y, z, and w vs. log of hydrogen column density.

Ideally, to achieve the same optical depth at zero and higher turbulent velocity, a higher column density should be required for the latter case. However, this outcome gets reversed due to line interlocking of x, y, and z with other ions (e.g., Fe^{23+}, Cr^{22+}, and Fe^{22+}; see Paper I). The higher the turbulent velocity is, the higher the Doppler width of a line and the more pronounced the line interlocking effects will be. Total line-center optical depth will therefore increase with turbulent velocity rather than decrease, as Equation (3) suggests.

6.4. Interplay between Column Density and Metallicity

Figure 13 shows the line ratios relative to w as contour plots by varying the hydrogen column density and metallicity. In the low-column-density limit, the line ratios are minimally affected by the change in metallicity. Figure 6 shows the effects of metallicity on the line ratios at the reported value of hydrogen column density by Hitomi Collaboration et al. (2018b) ($N_{\rm H,hot} \sim 1.88 \times 10^{21}$ cm^{-2}). The uncertainties in temperature and collision strengths from the sources mentioned previously contribute to the uncertainties in the line ratios (shown with the solid enclosed lines in Figure 6). At the reported hydrogen column density, x, y, and z are optically thin (Paper I). Therefore, the line ratios are minimally affected with change in metallicity as these lines are still optically thin for the metallicity range ($0 \leqslant Z$(solar) $\leqslant 5$) shown in the figure.

Hitomi Collaboration et al. (2018a) use deprojected heavy element abundances relative to solar in the inner 150 kpc region from Chandra data archive for a spherically symmetric Perseus model. At a distance of 30–60 kpc from the central AGN of the Perseus core, the reported range in metallicity is ~0.5–0.75 of solar (see Figure 7 in their paper). We overplot the CLOUDY calculated line ratios with Hitomi observed line ratios, and obtain a region of overlap for all the metallicities between 0 and 5. This is consistent with the reported metallicity range for the

Table 4
List of Collision Strengths at 4 keV from Different Atomic Data Sets for $n = 2 \rightarrow 1$ Transitions in Fe XXV

Label	Transition	Collision Strengths				
		Whiteford et al. (2001)	A. D. Whiteford (2005)	A. Giunta (2012)	Si et al. (2017)	Difference
w	$2^1P \rightarrow 1^1S$	3.97e−3	3.99e−3	4.32e−3	4.18e−3	8%
x	$2^3P_2 \rightarrow 1^1S$	7.27e−4	7.39e−4	6.72e−4	7.13e−4	9%
y	$2^3P_1 \rightarrow 1^1S$	7.24e−4	7.31e−4	8.68e−4	7.90e−4	17%
⋯	$2^3P_0 \rightarrow 1^1S$	1.48e−4	1.48e−4	1.35e−4	1.51e−4	11%
z	$2^3S \rightarrow 1^1S$	3.05e−4	4.28e−4	2.46e−4	3.16e−4	42%
⋯	$2^1S \rightarrow 1^1S$	8.41e−4	8.59e−4	8.68e−4	1.05e−3	20%

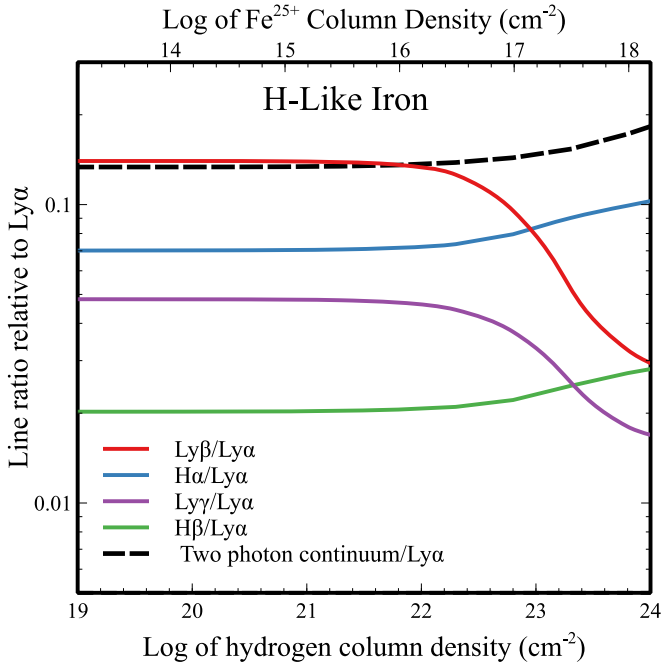

Figure 11. Fe XXVI line intensity ratios with respect to Lyα vs. log of hydrogen column density. The x-axis on top shows the log of Fe^{25+} column density. The dashed line is the integrated two-photon continuum relative to Lyα.

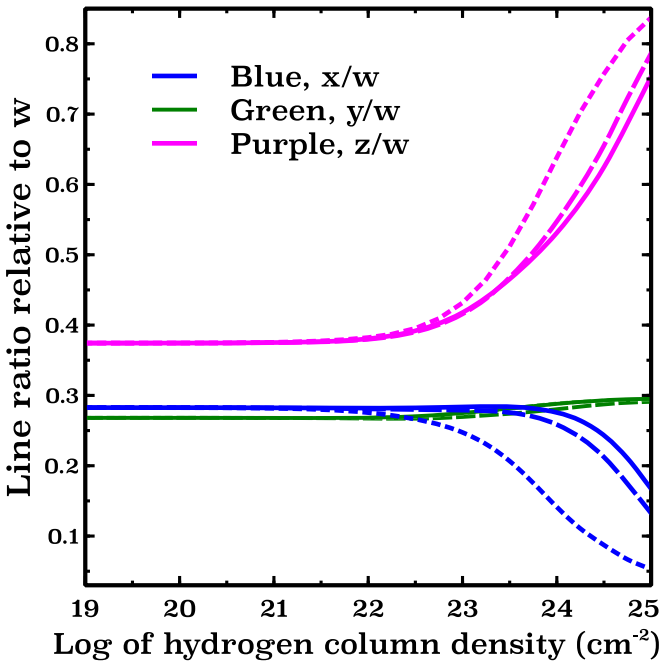

Figure 12. Line intensity ratio relative to w vs. log of hydrogen column density. Solid: no turbulence. Dashed: turbulence 150 km s^{-1}. Dotted: turbulence 500 km s^{-1}.

outer region of the Perseus core, but calculating/constraining the best-fit metallicity requires an extension of parameter space up to higher column densities.

In the high-column-density limit, the line ratios exhibit a clear variation with metallicity (see Figure 13). It can be seen that a smaller metallicity is equivalent to a larger hydrogen column density for the same optical depth. In systems with hydrogen column densities greater than 10^{23} cm^{-2}, like Seyfert 2 Galaxies (Risaliti et al. 1999; Terashima & Wilson 2001; Mocz et al. 2011), a comparison between the calculated and observed line ratios can be used to measure/constrain metallicities.

7. Summary

The next-generation microcalorimeter on board Hitomi made precision spectroscopy in X-rays possible for the first time. This enables us to explore radiative transfer effects like Case A to B transition in X-rays, previously observed in the optical/ultraviolet (Baker & Menzel 1938). In this paper, we document the Case A to B transition for H-like and He-like iron and show that it can be used to constrain column density. We also show the effect of turbulence, and the interplay between column density and metallicity in the outer region of the Perseus core using a line ratio diagnostic. In addition, we show that highly charged He-like systems behave differently from He I and other low-charge He-like systems. This is due to the atomic number dependence of transition probabilities, leading to fast transitions in unallowed triplet to singlet transitions.

From a comparison between the CLOUDY predicted and Hitomi observed line ratios in the outer region of Perseus core for the observed temperature, column density, and metallicity (see Figure 14), we find an agreement of ∼91%, 99%, and 98% in the x/w, y/w, and z/w ratios.

In the case B limit, two factors contribute to the variation in line ratios with column density for the same sets of physical parameters. First, line photons get absorbed in the cloud and are re-emitted as different lines (see Section 6.1.1). Second, line photons are absorbed in the cloud and re-emitted in a different direction, leading to the change in intensity of line photons along our line of sight (i.e., RS). Physically, it represents the migration of photons from the center of the cluster, where there is a photon deficit, to the outer regions, where there would be a photon surplus (Gilfanov et al. 1987). Our current model treats the cluster as a single sphere and cannot recover this physics

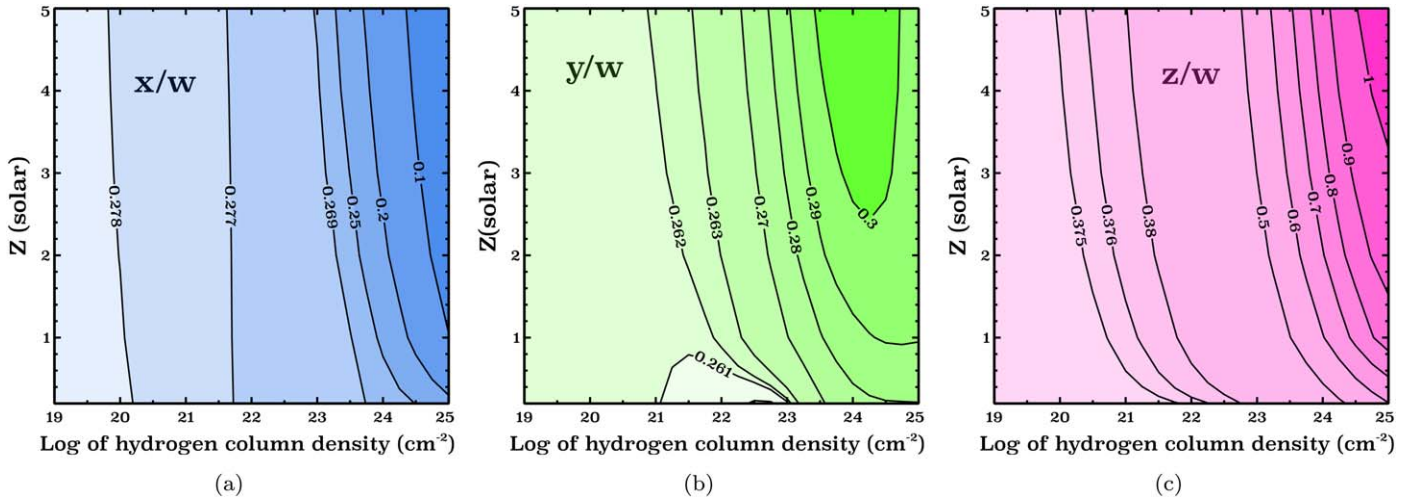

Figure 13. Left, middle, and right panels show x/w, y/w, and z/w as a function of hydrogen column density and metallicity, respectively.

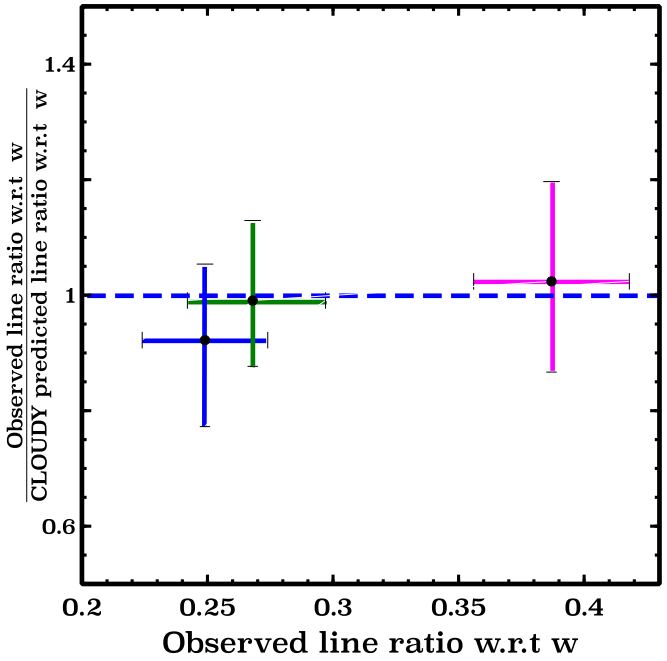

Figure 14. The ratio of observed to CLOUDY predicted line ratios plotted as a function of observed line ratios. All the ratios are taken with respect to the resonance (w) line. The points with red, blue, and purple error bars show the degree of agreement with the Hitomi observed line ratios for x/w, y/w, and z/w, respectively. Vertical error bars are calculated using observational and CLOUDY estimated uncertainties. The blue dotted line shows the ideal situation where observed line ratios exactly match with the predicted rate.

region-wise. A proper model of the variation in density and temperature across the cluster will be investigated in a later paper. The first line to become optically thick is w (see Figure 1(b) in Paper I). We use a flux suppression factor of ∼1.28 for w reported by Hitomi Collaboration et al. (2018a) at the outer region of Perseus core for the best-fit column density $N_{\rm H,hot} \sim 1.88 \times 10^{21}\,{\rm cm}^{-2}$ (Hitomi Collaboration et al. 2018b). Flux suppression in x, y, and z is insignificant at such a small column density, but it needs to be considered for higher column densities when these lines become optically thick.

In Section 6.2, we introduced a novel method of measuring/constraining column density from Case A to B transition. In the case of Perseus, x, y, and z are still in the optically thin regime (Case A). Therefore, we only get an upper limit in column density instead of a specific value. However, this method will be useful in systems with higher column densities ($N_{\rm H} \geqslant 10^{23}\,{\rm cm}^{-2}$) in the optically thick regime (Case B) for measuring column density.

The comments of John Raymond, the referee of this paper, were very helpful and added significantly to the presentation of our work. His help is gratefully acknowledged. We thank Stefano Bianchi, Andrew Fabian, and Anna Ogorzalek for their valuable comments. We acknowledge support by NSF (1816537, 1910687), NASA (17-ATP17-0141, 19-ATP19-0188), and STScI (HST-AR-15018). M.C. also acknowledges support from STScI (HST-AR-14556.001-A).

Software: Xspec (v12.10.1, Arnaud 1996), HEAsoft (v6.25, HEASARC 2014), CLOUDY (Ferland et al. 2017).

ORCID iDs

P. Chakraborty https://orcid.org/0000-0002-4469-2518
G. J. Ferland https://orcid.org/0000-0003-4503-6333
M. Chatzikos https://orcid.org/0000-0002-8823-0606
F. Guzmán https://orcid.org/0000-0002-2915-3612

References

Allen, C. W. 1973, Astrophysical Quantities (London: Athlone)
Allen, S. W. 2000, MNRAS, 315, 269
Arnaud, K. A. 1996, in ASP Conf. Ser. 101, XSPEC: The First Ten Years ed. G. H. Jacoby & J. Barnes (San Francisco, CA: ASP), 17
Badnell, N. R. 2006, A&A, 447, 389
Baker, J. G., & Menzel, D. H. 1938, ApJ, 88, 52
Baker, J. G., Menzel, D. H., & Aller, L. H. 1938, ApJ, 88, 422
Borgani, S. 1995, PhR, 251, 1
Cassano, R., & Brunetti, G. 2005, MNRAS, 357, 1313
Chakraborty, P., Chatterjee, S., Dutta, A., & Myers, A. D. 2018, PASP, 130, 064001
Chakraborty, P., Ferland, G. J., Chatzikos, M., Guzmán, F., & Su, Y. 2020, ApJ, 901, 68, (Paper I)
Churazov, E., Forman, W., Jones, C., & Böhringer, H. 2003, ApJ, 590, 225
Churazov, E., Forman, W., Jones, C., Sunyaev, R., & Böhringer, H. 2004, MNRAS, 347, 29
Dere, K. P., Landi, E., Mason, H. E., Monsignori Fossi, B. C., & Young, P. R. 1997, A&AS, 125, 149
Dubois, Y., Devriendt, J., Slyz, A., & Teyssier, R. 2010, MNRAS, 409, 985
Edge, A. C., Stewart, G. C., & Fabian, A. C. 1992, MNRAS, 258, 177
Elmegreen, B. G., Galliano, E., & Alloin, D. 2009, ApJ, 703, 1297

Fabian, A. 2012, ARA&A, 50, 455
Fabian, A. C. 1994, ARA&A, 32, 277
Feretti, L., Giovannini, G., Govoni, F., & Murgia, M. 2012, A&ARv, 20, 54
Ferland, G. J. 1999, PASP, 111, 1524
Ferland, G. J., Chatzikos, M., Guzmán, F., et al. 2017, RMxAA, 53, 385
Ferland, G. J., Porter, R. L., van Hoof, P. A. M., et al. 2013, RMxAA, 49, 137
Gilfanov, M. R., Syunyaev, R. A., & Churazov, E. M. 1987, SvAL, 13, 3
Guzmán, F., Chatzikos, M., van Hoof, P. A. M., et al. 2019, MNRAS, 486, 1003
Hitomi Collaboration, Aharonian, F., Akamatsu, H., et al. 2016, Natur, 535, 117
Hitomi Collaboration, Aharonian, F., Akamatsu, H., et al. 2018a, PASJ, 70, 10
Hitomi Collaboration, Aharonian, F., Akamatsu, H., et al. 2018b, PASJ, 70, 12
Hummer, D. G., & Storey, P. J. 1987, MNRAS, 224, 801
Johnson, W. R., Savukov, I. M., Safronova, U. I., & Dalgarno, A. 2002, ApJS, 141, 543
Kaastra, J. S., Mewe, R., & Nieuwenhuijzen, H. 1996, in 11th Coll. on UV and X-ray Spectroscopy of Astrophysical and Laboratory Plasmas, 411
Kalberla, P. M. W., Burton, W. B., Hartmann, D., et al. 2005, A&A, 440, 775
Kelley, R. L., Akamatsu, H., Azzarello, P., et al. 2016, Proc. SPIE, 9905, 99050V
Kramida, A., Ralchenko, Y., Nave, G., & Reader, J. 2018, in 49th Annual Meeting of the APS Division of Atomic, Molecular and Optical Physics Meeting Abstracts (College Park, MD: APS), M01.00004, http://meetings.aps.org/link/BAPS.2018.DAMOP.M01.4
Kunze, H.-J. 2009, Introduction to Plasma Spectroscopy, Springer Series on Atomic, Optical, and Plasma Physics, Vol. 56 (Berlin: Springer)
Landi, E., Dere, K. P., Young, P. R., et al. 2005, HiA, 13, 653
Lebedev, V. S., & Beigman, I. L. 1998, Physics of Highly Excited Atoms and Ions, Springer Series on Atoms and Plasmas, Vol. 22 (Berlin: Springer)
Li, Y., & Bryan, G. L. 2012, ApJ, 747, 26
Liedahl, D. A. 2005, in AIP Conf. Ser. 774, X-ray Diagnostics of Astrophysical Plasmas: Theory, Experiment, and Observation, ed. R. K. Smith (Melville, NY: AIP), 99
Lin, C. D., Johnson, W. R., & Dalgarno, A. 1977, PhRvA, 15, 154
Lodders, K., & Palme, H. 2009, M&PSA, 72, 5154
Martin, W., & Wiese, W. 2006, in Springer Handbook of Atomic, Molecular, and Optical Physics (New York: Springer), 175
McCourt, M. K. J. 2014, PhD thesis, Univ. of California
McNamara, B. R., & Nulsen, P. E. J. 2007, ARA&A, 45, 117
Mihalas, D. 1970, Stellar Atmospheres (San Francisco, CA: Freeman)
Mitchell, R. J., Culhane, J. L., Davison, P. J. N., & Ives, J. C. 1976, MNRAS, 175, 29P
Mocz, P., Lee, J. C., Iwasawa, K., & Canizares, C. R. 2011, ApJ, 729, 30
Molendi, S., & Pizzolato, F. 2001, ApJ, 560, 194
NASA High Energy Astrophysics Science Archive Research Center (HEASARC) 2014, HEAsoft: Unified Release of FTOOLS and XANADU, Astrophysics Source Code Library, ascl:1408.004
Osterbrock, D. E., & Ferland, G. J. 2006, Astrophysics of Gaseous Nebulae and Active Galactic Nuclei (Sausalito, CA: Univ. Science Books)
Peterson, J. R., & Fabian, A. C. 2006, PhR, 427, 1
Peterson, J. R., Kahn, S. M., Paerels, F. B. S., et al. 2003, ApJ, 590, 207
Planelles, S., Schleicher, D. R. G., & Bykov, A. M. 2016, in Multi-scale Structure Formation and Dynamics in Cosmic Plasmas, Space Science Series of ISSI, Vol. 51, ed. A. Balogh et al. (New York: Springer), 93
Porter, R. L., & Ferland, G. J. 2007, ApJ, 664, 586
Radburn-Smith, D. J., Lucey, J. R., Woudt, P. A., Kraan-Korteweg, R. C., & Watson, F. G. 2006, MNRAS, 369, 1131
Risaliti, G., Maiolino, R., & Salvati, M. 1999, ApJ, 522, 157
Ross, R. R., Fabian, A. C., & Brandt, W. N. 1996, MNRAS, 278, 1082
Sampson, D. H., & Zhang, H. L. 1988, ApJ, 335, 516
Sarazin, C. L. 2008, in Gas Dynamics in Clusters of Galaxies, Lecture Notes in Physics, Vol. 740, ed. M. Plionis, O. López-Cruz, & D. Hughes (Dordrecht: Springer), 24
Si, R., Li, S., Wang, K., et al. 2017, A&A, 600, A85
Storey, P. J., & Hummer, D. G. 1995, MNRAS, 272, 41
Terashima, Y., & Wilson, A. S. 2001, ApJ, 560, 139
Tugay, A. V., & Voytsehovsky, V. V. 2017, AstSR, 13, 81
Verner, D. A., Ferland, G. J., Korista, K. T., & Yakovlev, D. G. 1996, ApJ, 465, 487
Voronov, G. S. 1997, ADNDT, 65, 1
White, D. A., Jones, C., & Forman, W. 1997, MNRAS, 292, 419
Whiteford, A. D., Badnell, N. R., Ballance, C. P., et al. 2001, JPhB, 34, 3179
Zhuravleva, I., Churazov, E., Schekochihin, A. A., et al. 2014, Natur, 515, 85